# Chapter 2

## High Entropy Oxides and their Functional Properties

### 2.1 Introduction

The evolution of engineering materials over centuries is marked by a continuous trend of incorporating elements into a base material from bronze to cast iron to steel. This journey has been shaped by pivotal scientific milestones. In 1788, German scientist Karl Franz Achard pioneered alloys with up to seven principal elements, a groundbreaking effort later recognized by Smith in 1963 [51]. Another leap came with Greer's confusion principle, proposing that increasing elemental diversity boosts entropy, fostering amorphous structures [85]. Later, Cantor et al. [10]tested this principle by incorporating 16-20 elements in equimolar proportions which results in multiphase or even single phase, and these findings made the foundation for the introduction of HEA in 2004. Over the past century, significant efforts have focused on simplifying these complex ceramics into binary or ternary forms for diverse engineering applications. Research on multi-component ceramics began as early as 1964, though the concept of entropy stabilization only emerged in 2004-2005. This pivotal breakthrough marked the birth of high-entropy ceramics, extending the principles of high-entropy alloys (HEAs) [11–13,51] to ceramics by combining metallic and non-metallic elements. In 2015, Rost et al. [22] brought the concept of high-entropy-stabilized ceramics into the spotlight by successfully synthesising a high-entropy oxide (HEO) with phase pure rock-salt structure containing five equiatomic cations. This groundbreaking work marked a turning

point in the field of high-entropy ceramics [53,71], sparking a surge in research and publications on HEOs. HEOs stabilization concept is similar to that of HEAs [12,86] where increasing the number of cations increases the configurational entropy making the TΔS term greater than ΔH (**Figure 2.1a**).

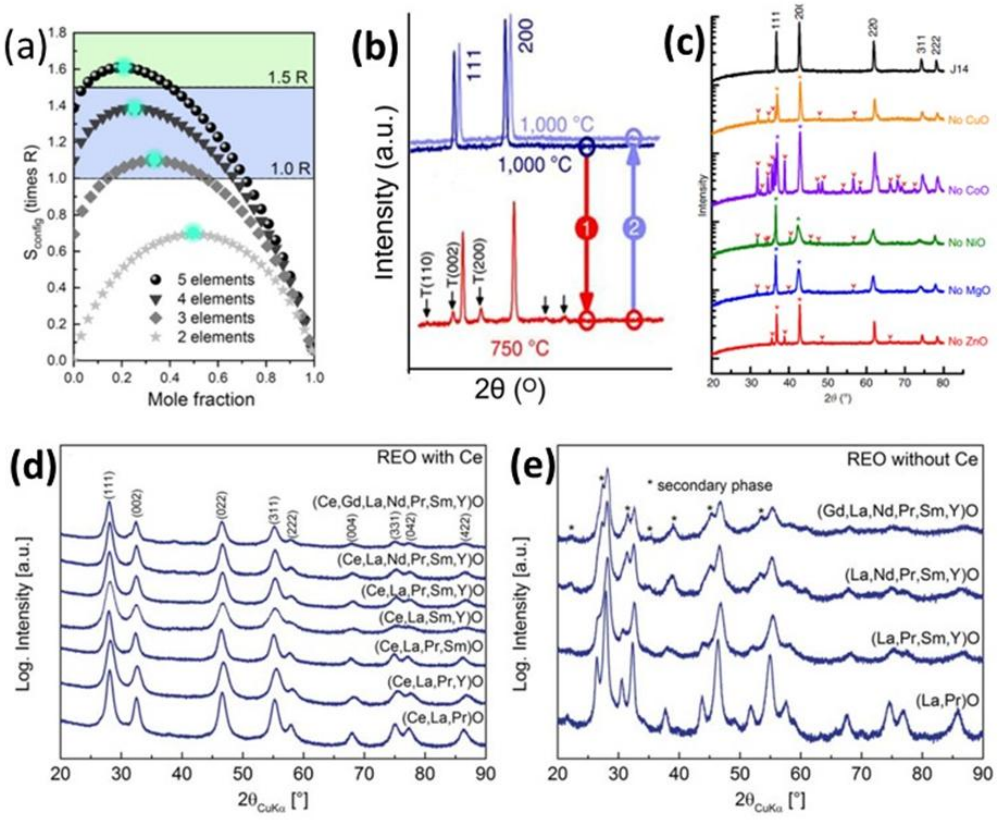


**Figure 2.1**(a) Correlation between configurational entropy ($S_{conf}$) and the number of elements and their respective mole fractions (b) XRD demonstrating reversibility which is an essential factor for entropy-stabilized oxides. (c) XRD pattern showing the role of individual cations in single-phase formation (d) XRD pattern showing the role of $Ce^{+4}$ in the design of single-phase fluorite HEOs. (e) Without $Ce^{+4}$ system crystallizes in multiphase oxides [22,47,57].

## 2.2 Entropy stabilized oxides (ESOs)

After the first report of HEO [22], the field of high entropy ceramics have been broadened to include nitrides [19], carbides [18,20], borides [18], and sulfides [21]. However, research in HEOs dominate over other high-entropy ceramics, driven by their fascinating scientific characteristics, unique properties, and broad potential applications, including thermal conductivity [66,73], catalysis [7,87–89], ionic conductivity [1,81,90,91], magnetic [69,92], mechanical [15,74,93] and electrical properties [1,94]. Rost et al. [22] were the first to explore entropy-driven phase stabilization by performing a reversibility test on transition-metal (TM) based rocksalt high entropy oxides (Mg,Co,Ni,Cu,Zn)O. On thermal cycling reversible phase transition was noticed in (Mg,Co,Ni,Cu,Zn)O when a single-phase rocksalt solid solution was obtained at high temperature while multiple phases (tenorite and wurtzite) evolved at lower temperatures [45]. The transition from single phase to multiphase and again to single phase on thermal cycling is shown in **Figure 2.1(b)** This phenomenon can be understood thermodynamically by considering the entropy-driven phase transition mechanism in which the entropy-dominated single phase solid solution is favoured at high temperatures and enthalpy-driven phase segregation occurs at lower temperatures as $\Delta G_{mix}$ form a single phase becomes positive [45,95]. The reversibility is not unique in high entropy oxides with >5 elements. Low and medium entropy oxides $(Ni_{0.2}Zn_{0.2})O$, $(Ni_{0.2}Cu_{0.2}Zn_{0.2})O$ also display reversibility albeit requires very high temperatures for the $-T\Delta S_{mix}$ term to more than compensate for the positive enthalpy ($\Delta H$) term [57]. Due to the significant role of entropy in phase stabilization, these oxide systems are also known as entropy-stabilized oxides (ESOs). Further, Rost et al. [22,96] also

highlighted the role of individual cations in the stability landscape of (Mg,Co,Ni,Cu,Zn)O as shown in **Figure 2.1c**, which illustrates that removing any constituent cation results in evolution of minor phase at 900-1000°C. Similar observations were also done by Fracchia et al. [97]and Salian et al. [46]. **Table 2.1** highlights different HEO exhibiting entropy driven phase stabilization. Several researchers [96] have examined the homogeneity and local structure of these HEOs using the X-ray absorption fine structure (XAFS) study [24]. Experimental scattering data confirmed that the rocksalt structure exhibited slight local disorder [49,98]. Additionally, an anion and cation sublattice showed oxygen/metal ions displaced from their ideal positions, causing distortions in the cation polyhedral. For a multicomponent composition to crystallize in a single-phase fluorite structure. cerium (Ce) and zirconium (Zr) elements are considered crucial. Rare-earth (RE) based systems without Ce or Zr always results in multiple phases [47],(shown in **Figure 2.1 (d,e)**) regardless of the number of incorporated elements or synthesis parameter. $Ce^{+4}$, $Zr^{+4}$ being an essential element in $(Ce_{0.2}La_{0.2}Pr_{0.2}Sm_{0.2}Y_{0.2})O_{2-\delta}$ and $(Zr_{0.2}La_{0.2}Pr_{0.2}Sm_{0.2}\ Y_{0.2})\ O_{2-\delta}$ , this might be due to their stable +4 oxidation state. However, more study is needed to explore the stability mechanism in high entropy fluorite structure. There are some general combination rules for the formation of single-phase high entropy fluorite oxides. The most well-known include $(CeRE)O_{2-\delta}$ and $(HfZrCeM)O_{2-\delta}$ [46,53,57]. In these general formulas, RE stands for rear earth elements such as La, Pr, Sm, Y, etc. and M stands for other metals whereas δ depends on cation valence.

**Table 2.1** Various published single-phase compositions in different crystal structures. The table also depicts a clear distinction between entropy-driven oxides and non-entropy-stabilized oxides.

| HEOs Compositions | | Entropy stabilization | Literature reference |
|---|---|---|---|
| | Rocksalt type HEOs | | |
| $(Co_{0.2}Cu_{0.2}Mg_{0.2}Ni_{0.2}Zn_{0.2})O$ (Several derivatives of this system contain additional elements like Li, Na, Ga, and K ) | | Yes | [99–103] |
| | Fluorite type HEOs | | |
| $(Ce_{0.2}La_{0.2}Pr_{0.2}Sm_{0.2}Y_{0.2})O_{2-\delta}$ | | No | [104] |
| $(Nd_{0.16}Ce_{0.16}La_{0.16}Pr_{0.16}Sm_{0.16}Y_{0.16})O_{2-\delta}$ | | No | [105] |
| $(Ce_{0.2}\ Zr_{0.2}\ Hf_{0.2}\ Sn_{0.2}\ Ti_{0.2})O_{2-\delta}$ | | Yes | [106] |
| | Perovskite type HEOs | | |
| $Ba(Zr_{0.2}\ Hf_{0.2}\ Sn_{0.2}\ Ti_{0.2}\ Nb_{0.2})O_3$ | | No* | [107] |
| $Sr(Zr_{0.2}\ Hf_{0.2}\ Sn_{0.2}\ Ti_{0.2}\ Nb_{0.2})O_3$ | | No | [108] |
| $(Gd_{0.2}La_{0.2}Nd_{0.2}Sm_{0.2}Y_{0.2})MnO_3$ | | Yes | [109] |
| | Spinel type HEOs | | |
| $(Co_{0.2}Cr_{0.2}Fe_{0.2}Mn_{0.2}Ni_{0.2})_3O_4$ | | No | [29] |

In the other general formula $RE_2TM_2O_7$, single phase high entropy fluorite structure forms when the ratio of ionic radius of the RE cation to that of the TM cation is equal to 1.46 [110].

## 2.3 Synthesis method for HEO

Various synthesis methods have been utilized for the fabrication of different HEOs shown in **Figure 2.2(a-f)**. Solid state reaction method [2,22] is most commonly utilized technique for the synthesis of high entropy oxides. This technique involves thorough mixing of raw powder of metal oxides followed by high temperature calcination. Rost et al. [22] was the first to employed SSR method to fabricate (Mg,Co,Ni,Cu,Zn)O HEO. Chen et. al used modified mechanochemical approach for the synthesis of five component rocksalt HEO at room temperature without need for post calcination.

Spark Plasma Sintering (SPS) is a rapid and efficient technique that processed powder materials by combining pulsed electric currents and mechanical pressure [75]. The electric current generates localized heat at particle contact points, briefly melting their surfaces to form a transient liquid phase, while the pressure drives rapid densification. This powerful synergy produces high dense structures in a fraction of the time required by traditional sintering methods. For instance, $Sr((Zr_{0.94}Y_{0.06})_{0.2}Sn_{0.2}Ti_{0.2}Hf_{0.2}Mn_{0.2})O_{3-\delta}$ synthesized via SPS for just 9 minutes at 1475 °C showed a significantly denser microstructure compared to the same material produced by a conventional solid-state reaction [40]. Reactive flash sintering on the other hand which was earlier used to synthesized $TiO_2$, ZnO,and $ZrO_2$ also used to synthesized High entropy oxides low temperature in short time

(**Figure 2.2c**). Kumar et al. [77] synthesized (Mg,Co,Ni,Cu,Zn)O with a single-phase rocksalt structure at the low temperature of 623 K in 3 min, In contrast, conventional thermal methods for producing this HEO typically need temperatures exceeding 1123 K and processing times of several hours. Mao et al. [111] fabricated $(La_{0.2}\ Nd_{0.2}Sm_{0.2}Eu_{0.2}Gd_{0.2})Zr_2O_7$ using reactive flash sintering in just seconds at 1200°C and highlighted microstructural evolution and studied mechanical properties showing fracture toughness 2.8 ±0.2 $MPa.m^{1/2}$. Ma et al. [112] analyzed the reactive flash sintering of $(Mg,Co,Ni,Cu,Zn)_xLi_{1-x}O$ and electrical transport properties of synthesized pallet were investigated and shows mixed ionic and electronic conductivity. Manchon et al. [113] conducted flash sintering of quinary HEO derived from Co-Cu-Fe-Mg-Mn-Ni-O and explored that both spinel and rocksalt phase obtained when flash sintered at atmospheric condition, however (Mg,Co,Ni,Cu,Zn)O exhibited single phase rocksalt structure.

Nebulized spray pyrolysis (NSP) is a versatile technique for synthesizing high entropy oxides with controlled composition and morphology [114–116]. In this method, a precursor solution containing metal salts is atomized into fine droplets using a nebulizer. These droplets are carried by a gas stream into hot wall reactor chamber (**Figure 2.2e**), where they undergo rapid thermal decomposition and chemical reactions, leading to the formation of HEO nanoparticles or thin films. The process enables precise control over stoichiometry, particle size, and homogeneity, making it ideal for producing advanced materials with tailored properties. On the other hand, in flame spray pyrolysis (FSP) [57,114] liquid metals with an oxidizing gas are sprayed into a flame zone where the metal oxides are

produced by combustion. This method has short rection time compared to NSP. In reverse co precipitation (RCP) technique solution of metal salts is mixed [114], followed by the controlled addition of an alkaline precipitant like sodium hydroxide or ammonia to simultaneously precipitate metal hydroxides. Key parameters, such as the precipitant addition rate, pH, and temperature, are meticulously adjusted to ensure the homogeneity of the precursor. The precipitates are then filtered, washed to eliminate impurities, and dried. Finally, calcination at high temperatures drives solid-state reactions and crystallization, yielding highly uniform HEOs. Sarkar et al. [117] successfully synthesized (Mg,Co,Ni,Zn)O and (Mg,Co,Ni,Cu,Zn)O entropy-stabilized oxides with a rocksalt structure using three distinct methods including NSP, FSP, and RCP. Their study demonstrated that the rock-salt crystal structure is independent of the synthesis method. Notably, the rocksalt phase formed directly after nebulized spray pyrolysis, whereas additional heat treatment was required to stabilize the phase following synthesis via flame spray pyrolysis and reverse co-precipitation.

Solution combustion synthesis (SCS) is widely used techniques for synthesizing oxides as it doesn't require any complex setup. SCS begin with the dissolution of metal precursors in solvent and fuel such as citric acid, glycine followed by gelation [118,119]. The gel is then heated in which self-sustaining exothermic reaction takes place and forms HEOs after calcination (**Figure 2.2b**). HEOs with varying crystal structures have been synthesized using SCS. For instance Mao et al. synthesized (Mg,Co,Ni,Cu,Zn)O rocksalt HEO [29] and $(Co_{0.2}\ Cr_{0.2}\ Fe_{0.2}\ Mn_{0.2}\ Ni_{0.2}\ )_3O_4$ spinel

HEO [65], Salian et al. [46] synthesized $(Ce_{0.2}La_{0.2}Pr_{0.2}Sm_{0.2}Y_{0.2})O_{1.6-\delta}$ perovskite HEOs and explored its electrical properties.

Several reports have been published on synthesis of high entropy oxides using hydrothermal techniques in which reaction proceeds in sealed autoclave reactor under high temperature and pressure. The morphology and particle size of the powder can be controlled by various parameters such as temperature, pH, and surfactant addition. For example, Yu. et al. [120] synthesized $(Ba_{0.2}Mg_{0.2}Ca_{0.2}Sr_{0.2}Pb_{0.2})TiO_3$ high entropy perovskite oxide and the effects of reaction temperature, time and pH value of hydrothermal reaction on phase and morphology of the powders were studied.

Pulsed Laser Deposition (PLD) is a versatile technique for fabricating thin films, now widely employed to synthesize simple and complex oxides [78]. A high-power laser ablates material from a target surface, generating a plasma plume through melting, evaporation, and ionization. The evaporated material then condenses onto a substrate, forming a film (**Figure 2.2f**) This process can be conducted in vacuum or with oxygen to tailor the growth of oxide films. Meisenheimer et al. [121] and Kotsonis et al. [122] utilized pulsed laser deposition to fabricate $(Mg_{0.25(1-x)}Co_xNi_{0.25(1-x)}Cu_{0.25(1-x)}Zn_{0.25(1-x)})O$ and $Mg_xNi_xCo_xCu_xZn_xSc_xO$, respectively. In both studies, pressed and sintered oxide mixtures served as targets, which as ablated using a 248-nm KrF laser beam. **Table 2.2** summarize the various synthesis methods utilized for different high entropy oxides.

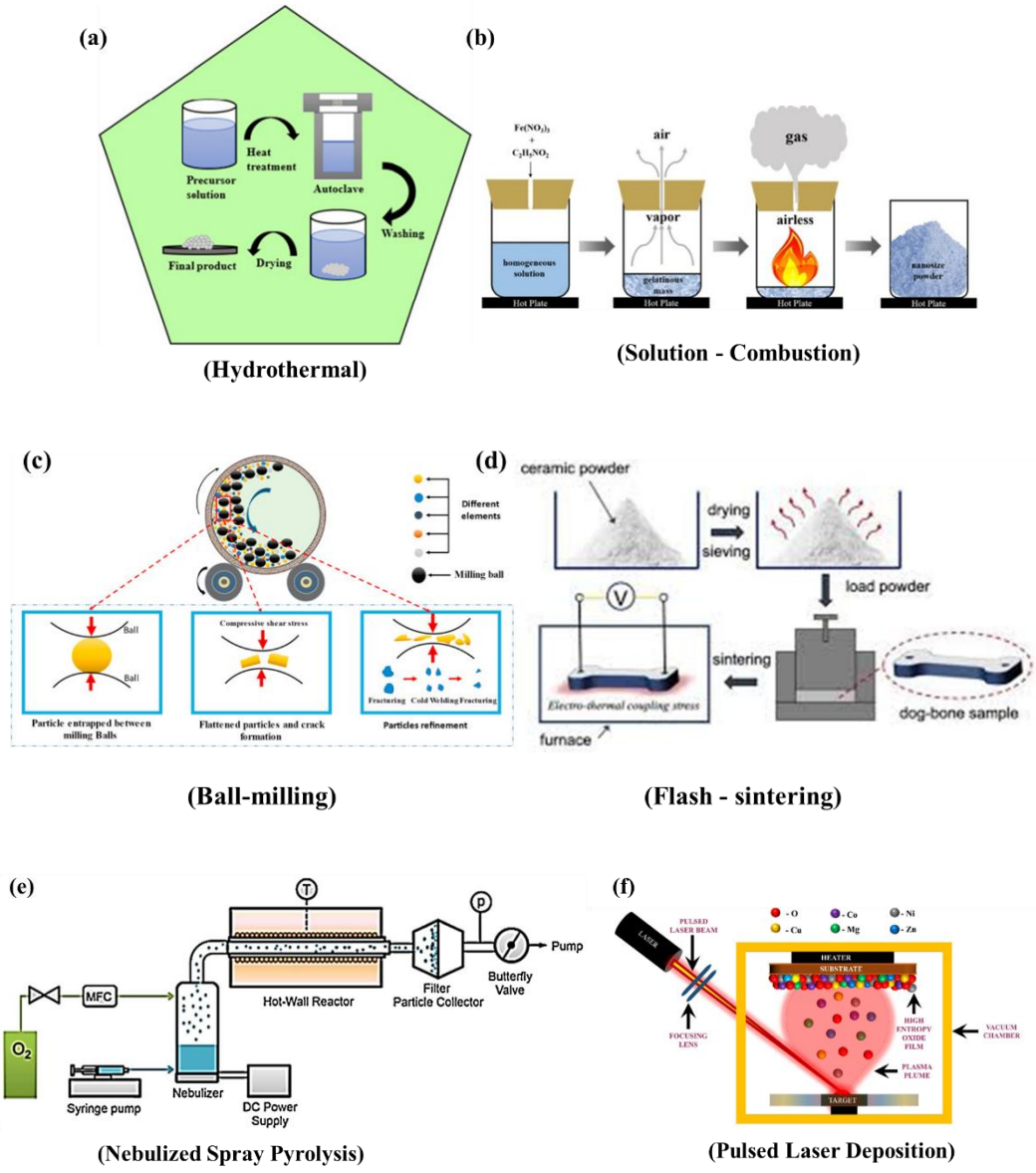


**Figure 2.2** The different synthesis techniques for the synthesis of high entropy oxides [57,76,78,123,124].

Overall, each synthesis method offers a distinct balance of advantages and limitations, making the choice highly dependent on the desired characteristics of the high entropy materials (HEMs) and the intended application.

**Table 2.2** Various synthesizing routes for different HEO compositions with their crystal structure.

| Synthesis method | HEOs composition | Crystal structure | Reference |
|---|---|---|---|
| Solid state reaction | | | |
| | $(Co_{0.2}\ Cu_{0.2}\ Mg_{0.2}\ Ni_{0.2}\ Zn_{0.2})O$ | Rocksalt | [22,74,125–127] |
| | $(Co_{0.2}\ Cr_{0.2}\ Fe_{0.2}\ Mn_{0.2}\ Ni_{0.2}\ )_3O_4$ | Spinel | [26] |
| | $(Co_{0.2}\ Fe_{0.2}\ Mn_{0.2}\ Ni_{0.2}\ Zn_{0.2})Fe_2O_4$ | Spinel | [128] |
| | $(Zn_{0.2},Fe_{0.2},Ni_{0.2}Mg_{0.2}Cd_{0.2})O_4$ | Spinel | [129] |
| | $(Mg_{0.2}\ Co_{0.2}\ Ni_{0.2}\ Cu_{0.2}\ Zn_{0.2})Cr_2\ O_4$ | Spinel | [128] |
| | $(Mg_{0.2}\ Co_{0.2}\ Ni_{0.2}\ Cu_{0.2}\ Zn_{0.2})Al_2\ O_4$ | Spinel | [128] |
| | (La) (Cr Fe Co Mn Ni) $O_3$ | Perovskite | [130] |
| | Ba (Zr Sn Ti Hf Me) $O_3$ Me = Y, Nb, S | Perovskite | [68] |
| | Sr (Ti Fe Mo Nb Cr) $O_3$ | Perovskite | [37] |
| | $(Ce_{0.5}\ Zn_{0.1}\ Co_{0.1}\ Mg_{0.1}\ Ni_{0.1}\ Cu_{0.1})\ O_x$ | Fluorite | [82] |
| | (Ce Gd La Nd Pr Sm Y)O | Fluorite | [32] |
| | Ba $(Fe_6\ Cr_{1.2}\ Ti_{1.2}\ In_{1.2}\ \ Ga_{1.2}\ Co_{1.2})\ O_{19}$ | Magnetoplumbit | [72] |
| | $(Yb_{0.2}\ Tb_{0.2}\ Gd_{0.2}\ Dy_{0.2}\ Er_{0.2})_2Ti_2\ O_7$ | Pyrochlore | [36] |
| Ball milling | | | |
| | $(Co_{0.2}\ Cu_{0.2}\ Mg_{0.2}\ Ni_{0.2}\ Zn_{0.2})O$ | Rocksalt | [2,126] |
| | $(Mg\ Co\ Ni\ Zn)_{1-x}\ Li_x\ O$ ( x = 0.05, 0.15, 0.025, 0.35) | Rocksalt | [1,2,22] |
| | $(Co_{0.2}\ Cr_{0.2}\ Fe_{0.2}\ Mn_{0.2}\ Ni_{0.2}\ )_3O_4$ | Spinel | [30] |
| | $(Co_{0.2}\ Cr_{0.2}\ Fe_{0.2}\ Mn_{0.2}\ Mg_{0.2}\ )_3O_4$ $(Cr_{0.2}\ Fe_{0.2}\ Mn_{0.2}\ Mg_{0.2}\ Ni_{0.2})_3O_4$ | Spinel | [27] |
| | Sr $(Zr_{\ 0.2}\ Sn_{0.2}\ Ti_{0.2}\ Hf_{0.2}\ Mn_{0.2})\ O_3$, Sr $(Zr_{\ 0.2}\ Sn_{0.2}\ Ti_{0.2}\ Hf_{0.2}\ Nb_{0.2})\ O_3$, Ba $(Zr_{\ 0.2}\ Sn_{0.2}\ Ti_{0.2}\ Hf_{0.2}\ Ce_{0.2})\ O_3$, $(Sr_{0.5}\ Ba_{0.5}\ )(Zr_{\ 0.2}\ Sn_{0.2}\ Ti_{0.2}\ Hf_{0.2}\ Nb_{0.2})\ O_3$ | Perovskite | [39,131] |
| | Ba $(Zr_{\ 0.2}\ Sn_{0.2}\ Ti_{0.2}\ Hf_{0.2}\ Nb_{0.2})\ O_3$ Ba $(Zr_{\ 0.2}\ Sn_{0.2}\ Ti_{0.2}\ Hf_{0.2}\ Y_{0.2})\ O_{3-x}$ | Perovskite | [41] |
| Mechanical Grinding | | | |
| | $(Co_{0.2}\ Cu_{0.2}\ Mg_{0.2}\ Ni_{0.2}\ Zn_{0.2})O$ $(Mg\ Co\ Ni\ Zn)_{1-x}Li_x\ O$, x= 0 .05, 1 $(Mg\ Co\ Ni\ Zn)_{1-2x}Li_x\ Ga_x\ O$ | Rocksalt | [2,132] |
| NSP | | | |
| | $(Co_{0.2}\ Cu_{0.2}\ Mg_{0.2}\ Ni_{0.2}\ Zn_{0.2})O$ | Rocksalt | [47,117] |
| | $(Zn_{0.25}\ Ni_{0.2}\ Co_{0.25}\ Mg_{0.25})O$, (Co,Cu,Mg,Ni,Zn,Na)O | Rocksalt | [83] |

| Synthesis method | HEOs composition | Crystal structure | Reference |
|---|---|---|---|
| | $(NiFeMnCrCo)_xO_y$<br>$(NiFeMnCrMg)_xO_y$<br>$(NiFeMnZnMg)_xO_y$ | Spinel | [28] |
| | $(Ce_{0.2}La_{0.2}Pr_{0.2}Sm_{0.2}Y_{0.2})\ O_{2-\delta}$ | Fluorite | [110] |
| | $(Gd_{0.2}\ La_{0.2}\ Nd_{0.2}\ Sm_{0.2}\ Y_{0.2})$<br>$(Co_{0.2}\ Cr_{0.2}\ Fe_{0.2}\ Mn_{0.2}\ Ni_{0.2})O_3$ | Perovskite | |
| | $(Gd_{0.2}\ La_{0.2}\ Nd_{0.2}\ Sm_{0.2}\ Y_{0.2})\ Co\ O_3$<br>$(Gd_{0.2}\ La_{0.2}\ Nd_{0.2}\ Sm_{0.2}\ Y_{0.2})\ Cr\ O_3$<br>$(Gd_{0.2}\ La_{0.2}\ Nd_{0.2}\ Sm_{0.2}\ Y_{0.2})\ Fe\ O_3$ | Perovskite | [44,47] |
| FSP | | | |
| | $(Co_{0.2}\ Cu_{0.2}\ Mg_{0.2}\ Ni_{0.2}\ Zn_{0.2})O$ | Rocksalt | [57] |
| | $(Gd_{0.2}\ La_{0.2}\ Y_{0.2}\ Hf_{0.2}\ Zr_{0.2})O_2$ | Fluorite | [47] |
| RCP | | | |
| | $(Co_{0.2}\ Cu_{0.2}\ Mg_{0.2}\ Ni_{0.2}\ Zn_{0.2})O$ | Rocksalt | [117] |
| Sol-gel | | | |
| | $(La_{0.2}Y_{0.2}Nd_{0.2}Gd_{0.2}Sr_{0.2})CrO_3$ | Perovskite | [133] |
| | $(La_{0.2}Pr_{0.2}\ Nd_{0.2}\ Sm_{0.2}\ Sr_{0.2})Mn\ O_{3-\delta}$ | Perovskite | [44] |
| SCS | | | |
| | $(Co_{0.2}\ Cu_{0.2}\ Mg_{0.2}\ Ni_{0.2}\ Zn_{0.2})O$ | Rocksalt | [29] |
| | $(Co_{0.2}\ Cr_{0.2}\ Fe_{0.2}\ Mn_{0.2}\ Ni_{0.2}\ )_3O_4$ | Spinel | [65] |
| | $(Cr_{0.2}\ Fe_{0.2}\ Mn_{0.2}\ Ni_{0.2}\ Zn_{0.2}\ )_3O_4$<br>$(Cr_{0.2}\ Fe_{0.2}\ Mn_{0.2}\ Co_{0.2}\ Zn_{0.2}\ )_3O_4$ | Spinel | [65,134] |
| | $(Al_{1/6}\ Co_{1/6}\ Cr_{1/6}\ Fe_{1/6}\ Mn_{1/6}\ Ni_{1/6})_3O_4$ | Spinel | [135] |
| PLD | | | |
| | $(Co_{0.2}\ Cu_{0.2}\ Mg_{0.2}\ Ni_{0.2}\ Zn_{0.2})O$ | Rocksalt | [136] |
| | $(Mg_{0.25(1-x)}\ Co_x\ Cu_{0.25(1-x)}\ Ni_{0.25(1-x)}$<br>$Zn_{0.25(1-x)})O$, x = 0.2, 0.27, 0.33 | Rocksalt | [136] |
| | $(Co_{0.167}\ Cu_{0.167}\ Mg_{0.167}\ Ni_{0.167}\ Zn_{0.167}$<br>$Sc_{0.167})\ O$,<br>$(Co_{0.167}\ Cu_{0.167}\ Mg_{0.167}\ Ni_{0.167}\ Zn_{0.167}$<br>$Li_{0.167})\ O$,<br>$(Co_{0.167}\ Cu_{0.167}\ Mg_{0.167}\ Ni_{0.167}\ Zn_{0.167}$<br>$Ge_{0.167})\ O$, | Rocksalt | [137] |
| | $(Co_{0.167}\ Cu_{0.167}\ Mg_{0.167}\ Ni_{0.167}\ Zn_{0.167}$<br>$Cr_{0.167})\ O$,<br>$(Co_{0.167}\ Cu_{0.167}\ Mg_{0.167}\ Ni_{0.167}\ Zn_{0.167}$<br>$Sb_{0.167})\ O$,<br>$(Co_{0.167}\ Cu_{0.167}\ Mg_{0.167}\ Ni_{0.167}\ Zn_{0.167}$<br>$Sn_{0.167})\ O$, | Rocksalt | [136] |
| | $(Mg_{0.2}Ni_{0.2}Fe_{0.2}Co_{0.2}Cu_{0.2})Fe_2O_4$ | Spinel | [80] |
| | $Ba\ (Zr_{0.2}\ Sn_{0.2}\ Ti_{0.2}\ Hf_{0.2}\ Nb_{0.2})\ O$ | Perovskite | [38] |

| Synthesis method | HEOs composition | Crystal structure | Reference |
|---|---|---|---|
| Magnetron sputtering | | | |
| | (Al Cr Fe Ni Mn) O | Rocksalt | [138] |
| Flash assisted synthesis | | | |
| | $(Co_{0.2}\ Cu_{0.2}\ Mg_{0.2}\ Ni_{0.2}\ Zn_{0.2})O$ | Rocksalt | [77] |
| | $Sr\ (Zr_{\ 0.2}\ Sn_{0.2}\ Ti_{0.2}\ Hf_{0.2}\ Y_{0.2})\ O_{3-x}$ | Perovskite | [139] |
| | $(Bi_{0.2}\ Na_{0.2}\ \ K_{0.2}\ \ Ba_{0.2}\ \ Ca_{0.2})\ Ti\ O_3$ | Perovskite | [140] |
| Hydrothermal | | | |
| | $(Co_{0.2}\ Cu_{0.2}\ Mg_{0.2}\ Ni_{0.2}\ Zn_{0.2})O$ | Rocksalt | [95] |
| Solvothermal | $(Co_{0.2}\ Fe_{0.2}\ Cr_{0.2}\ Mn_{0.2}\ Ni_{0.2})_3\ O_4$ | Spinel | [28] |
| Epitaxial film synthesis | | | |
| | $(Mg_{0.25(1-x)}\ \ Cu_x\ \ Co_{0.25(1-x)}\ \ Ni_{0.25(1-x)}\ Zn_{0.25(1-x)})O$, x = 0.11, 0.17, 0.20, 0.24 | Rocksalt | [122] |
| Sono-chemical | | | |
| | $BaSr(ZrHfTi)O_3$, $BaSrBi(ZrHfTiFe)O_3$ and $Ru/BaSrBi(ZrHfTiFe)O_3$ | Perovskite | [141] |

## 2.4 Isovalent and aliovalent addition in HEOs

As discussed earlier, the basic criteria for the selection of cations were based on Paulling's rules that emphasises on the neighbouring ionic radii, same coordination number for a particular lattice structure, and the same oxidation state [116,142]. The initial research on HEOs concentrated primarily on rocksalt systems with a single Wyckoff site for the cations. Adding sixth cation in the lattice, entropy contribution increases undoubtedly. Partial substitution either by isovalent or aliovalent elements in (Mg,Co,Ni,Cu,Zn)O involve charge compensation mechanisms that help in maintaining the charge neutrality which facilitates a wide range of phase pure compositions and tailoring their properties.

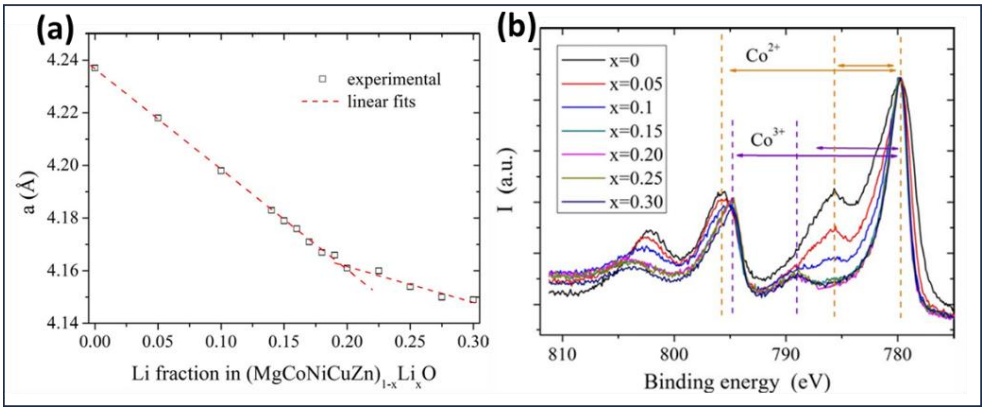


**Figure 2.3**(a) The linear relation between the lattice parameter of (Co, Mg, Ni, Cu, Zn)$_{1-x}$Li$_x$O HEOs and the concentration of lithium. Two distinct slopes indicate two compensation mechanisms involved for single phase HEOs formation (b) XPS spectra of Co 2p showing that all the Co present in divalent state converted to $Co^{+3}$ at (x=0.2) Lithium concentration [81].

Ionic charge balance and geometrical compatibility both must be considered when designing HEOs. Compensation mechanisms are often accompanied by oxygen vacancies. When an isovalent cation such as calcium ($Ca^{2+}$) which has ionic radii ~1 Å is substituted to parent rocksalt (Mg,Co,Ni,Cu,Zn)O HEOs, large size of $Ca^{2+}$ limits its solubility in the lattice and about ~7% CaO is formed as a secondary phase [83]. However, $(Mg,Co,Ni,Cu,Zn)_{1-x}Ca_xO$ non-equimolar HEOs (NE-HEOs) with Ca doping ($x \leq 0.1$) have been synthesized and photocatalytic properties explored [143]. There are some reports which highlighted the aliovalent substitution in HEOs [56,80,81]. Substituting a part of +2 cations with $Li^{1+}$ (~0.76 Å) to form $(Mg,Co,Ni,Cu,Zn)_{1-x}Li_xO$ leads to a single phase rocksalt structure being maintained upto x=0.3. Since the ionic size of $Li^{1+}$ is slightly larger (in octahedral geometry) than the average ionic radius of 5 divalent cations in (Mg,Co,Ni,Cu,Zn)O. To accommodate $Li^{1+}$ in the lattice, oxidation of some divalent cations ($M^{2+}$) or the formation of oxygen vacancies take place. This defect reaction can be represented using Kröger–Vink notation as follows:

$$MO + Li_2O \rightarrow 2Li'_M + V_O^{\cdot\cdot} + 1/2\ O_2$$

**Figure 2.3(a)** shows two distinct regions with linear dependency of lattice parameters on the concentration of $Li^{1+}$. Two different slopes indicate that there might be two distinct charge compensation mechanisms involved. When the concentration of $Li^{1+}$ was x=0.21 introduced in (Mg,Co,Ni,Cu,Zn)O, the charges are first compensated by the oxidation of $Co^{2+}$ to oxidation of $Co^{3+}$ (**Figure 2.3b**)

[59]. Since $Co^{+3}$ is more stable in an octahedral environment than $Ni^{3+}$, a lesser fraction of Ni goes into $Ni^{3+}$ valence state. However, when the $Li^{1+}$ concentration was above the x=0.21 limit. the second mechanism comes into play in which all $Co^{2+}$ turns into $Co^{3+}$ and the creation of oxygen vacancies in the lattice takes place. When $Li^{1+}$ and $Ga^{3+}$ cations are co-substituted in (Mg,Co,Ni,Cu,Zn)O, single phase rocksalt $(Mg,Co,Ni,Cu,Zn)_{0.8}(LiGa)_{0.2}O$ HEOs is obtained [2]. In this case self-compensation by substituting cations comes into play which facilitates the partial substitution of $M^{2+}$ by +1 and +3 cations. The average ionic radius of $Li^{1+}$(~0.76 Å) and $Ga^{3+}$ (~ 0.62 Å) is smaller than the average ionic size of cations in (Mg,Co,Ni,Cu,Zn)O thus a significant decrease in lattice parameter compare to pristine HEOs is observed. However, when the $Ga^{3+}$ cation (smaller ionic size compared to the average ionic radius of the element in pristine HEOs is substituted independently it leads to the formation of secondary phases. Thus, the successful formation of a single-phase self-compensation mechanism is an important factor so that the combination of +1/+3 cation can substitute $M^{2+}$ lattice site. Another aliovalent cation sodium ($Na^{1+}$) has quite a large ionic radius (even greater than Hume-Rothery ±15% criteria) compared to the average size of the cation present in (Mg,Co,Ni,Cu,Zn)O [83]. Unexpectedly on substitution, it results in single-phase rocksalt (Mg,Co,Ni,Cu,Zn,Na)O at 1000°C. It is quite interesting to observe such a result where a large ionic size (~1.02 Å) aliovalent cation successfully crystalizes in a single phase at a somewhat higher temperature compared to that of pristine rocksalt HEOs. The lattice parameter after substitution decreases when compared to (Mg,Co,Ni,Cu,Zn)O. This indicates that geometrical and electrical charge compensation mechanisms come into play. From the XPS study shown in **Figure**

**2.4**, it is obvious that only oxygen vacancy formation is not sufficient to compensate for the aliovalent cations with large ionic sizes, cations like $Co^{2+}$, and $Ni^{2+}$ have to take higher oxidation states simultaneously. Oxidation of $Ni^{2+}$ can compensate only part of the substitution; the remaining can only be compensated by oxidation of $Co^{2+}$ [81]. Thus, Co becomes an essential element to maintain charge neutrality which results in single-phase rocksalt structure formation. It is also obvious from the XPS study that Cu can be present in both +1 and +2 oxidation states. Further, when a combination of $Na^{1+}$, and $Ga^{3+}$ is substituted in (Mg,Co,Ni,Cu,Zn)O, similar to $Li^{1+}$, $Ga^{3+}$ combination, a self-compensating mechanism should come into play

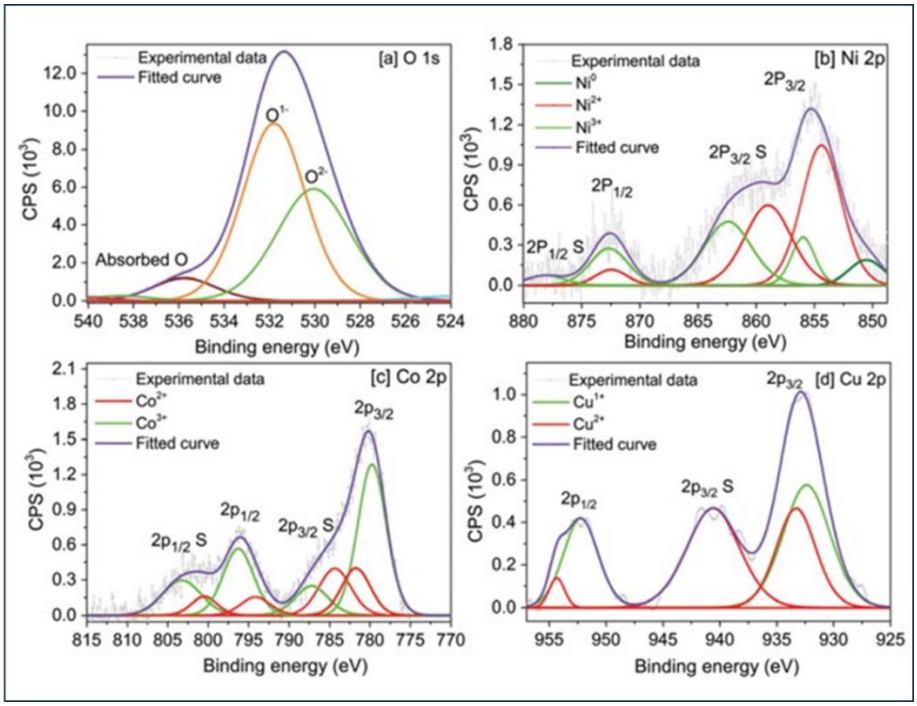


**Figure 2.4** XPS spectra of (a) O1s (b) Ni2p (c) Co 2p and (d) Cu 2p indicate charge compensation mechanism in single phase (Mg,Co,Ni,Cu,Zn,Na)O HEOs which include oxidation of divalent cation as well as the formation of oxygen vacancies [83].

for the formation of single phase $(Mg,Co,Ni,Cu,Zn)_{0.8}(NaGa)_{0.2}O$.The average ionic radius of $Na^{1+}$ (1.02 Å ) and $Ga^{3+}$ (~0.62 Å) is larger than the average ionic radius of cation in (Mg,Co,Ni,Cu,Zn)O, thus the lattice parameter of $(Mg,Co,Ni,Cu,Zn)_{0.8}(NaGa)_{0.2}O$ HEO increased significantly [56].

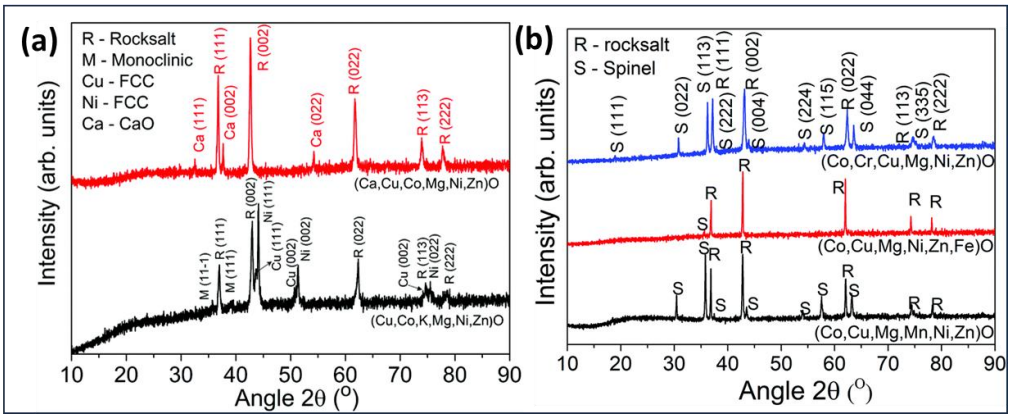


**Figure 2.5** Illustrates the stability landscape of (a) $Ca^{2+}$ (above) and $K^{1+}$ (bottom) addition (b) aliovalent addition ($Cr^{3+}$, $Fe^{3+}$, and $Mn^{3+}$) as sixth element in (Mg,Co,Ni,Cu,Zn)O [83].

Similar to these compositions we can design a wide range of compositions and thus engineer various properties by just knowing the crucial element for the charge compensating mechanism. Usharani et al. [83]concluded that although addition of $Fe^{3+}$, $Cr^{3+}$, $Mn^{3+}$, $Ca^{2+}$, or $K^{1+}$ in (Mg,Co,Ni,Cu,Zn)O as sixth cation, in equimolar proportions, increases configurational entropy; however, due to the formation of microstates and ordering, single phase was not obtained (**Figure 2.5 (a,b)**). The six component HEOs can form single phase on heating to higher temperatures; however, effect of calcination temperature on single-phase formation for these cation substitutions is not discussed in these reports.

## 2.5 Distortion in HEO

Berardan et al. [1,2] revealed a striking contrast in multi-component oxides, while systems like $(MgCoNiZn)_{0.8}(LiGa)_{0.2}$ exhibit no severe lattice distortion without CuO. The inclusion of CuO unlocks a unique structural phenomenon. $Cu^{2+}$ ions, in their octahedral coordination, shows Jahn-Teller distortion of the oxygen sublattice, creating a distinctive pattern of four short and two long Cu-O bonds [49,96,97]. While the simple crystal structure precludes cooperative distortion across all octahedra, localized structural displacements hold the potential to revolutionize the functional properties of these materials. For instance, exceptional dielectric constants across frequencies and room-temperature fast ion conductivity. Jahn-Teller effects in transition metal oxides can introduce anisotropic transport properties [144], and studies have shown that functional properties, such as resistivity and dielectric constant, can be fine-tuned by controlling the degree of distortion [112,145]. This underscores the importance of understanding the structural behaviour to unlock the full potential. Similarly large or small size cation addition results in strain in the lattice and transform the lattice from ideal rocksalt to distorted rocksalt which could influence the function properties. **Figure 2.6a** shows a schematic of the nature of distortion in HEOs. Despite its fundamental importance, however, lattice distortion in HEOs remains an open issue, yet to be fully understood. In the case of HEAs [53,86], a series of innovative experiments has been proposed to unravel and validate the concept of lattice distortion. Early attempts to characterize lattice distortion in HEAs relied on X-ray diffraction, with the assumption that large distortions would weaken diffraction peak intensities. While initial results showed peak intensity reduction with an increasing number of

elements [146], the findings were later contested due to the influence of thermal vibrations and crystallographic texture. High-resolution transmission electron microscopy (HRTEM) was also employed, but interpreting curved atomic planes in images proved challenging, as such features could arise from strain fields around defects rather than lattice distortion [147]. More recent studies have used advanced methods to refine our understanding. Owen et al. [148] applied neutron diffraction to HEAs like Ni, CrNi, CoCrNi, and CoCrFeMnNi, observing greater lattice strain in CoCrFeMnNi compared to pure Ni, though the differences among HEAs were minimal. Similarly, Tong et al. [149] quantified local lattice distortions using X-ray diffraction and extended X-ray absorption fine structure, finding small distortions in CoCrFeNi and CoCrFeMnNi, but more pronounced distortion in CoCrFeNiPd due to larger atomic size of Pd. Usharani et al. [115] highlighted the distortion due to magnetostriction in (Mg,Co,Ni,Cu,Zn)O, which results in transforming the ideal rocksalt structure to monoclinic as shown in **Figure 2.6b**. They concluded that distortion was primarily due to the antiferromagnetism originating from constituent binary oxides such as CoO, NiO [150]. However, they didn't discuss the distortion due to ionic size mismatch. Further, the varying magnitudes of lattice stress experienced by distinct size of cation lead to lattice distortion in high-entropy oxides (HEOs) [98,148,151]. In the solid solution phase, each atom is surrounded by neighbouring atoms of different sizes, creating an uneven lattice strain. Unlike conventional oxides, where adjacent atoms are mostly of the same or similar species, HEOs exhibit significant asymmetry and structural anomalies. In semiconductors, electron waves formed by carrier movement are scattered due to lattice distortions. This increases the probability of collisions between carriers and

lattice atoms, leading to greater scattering and reduced mobility. Lower mobility results in decreased conductivity, causing carriers to accumulate. This accumulation contributes to enhanced dielectric performance [145], making HEOs promising for applications requiring superior dielectric properties.

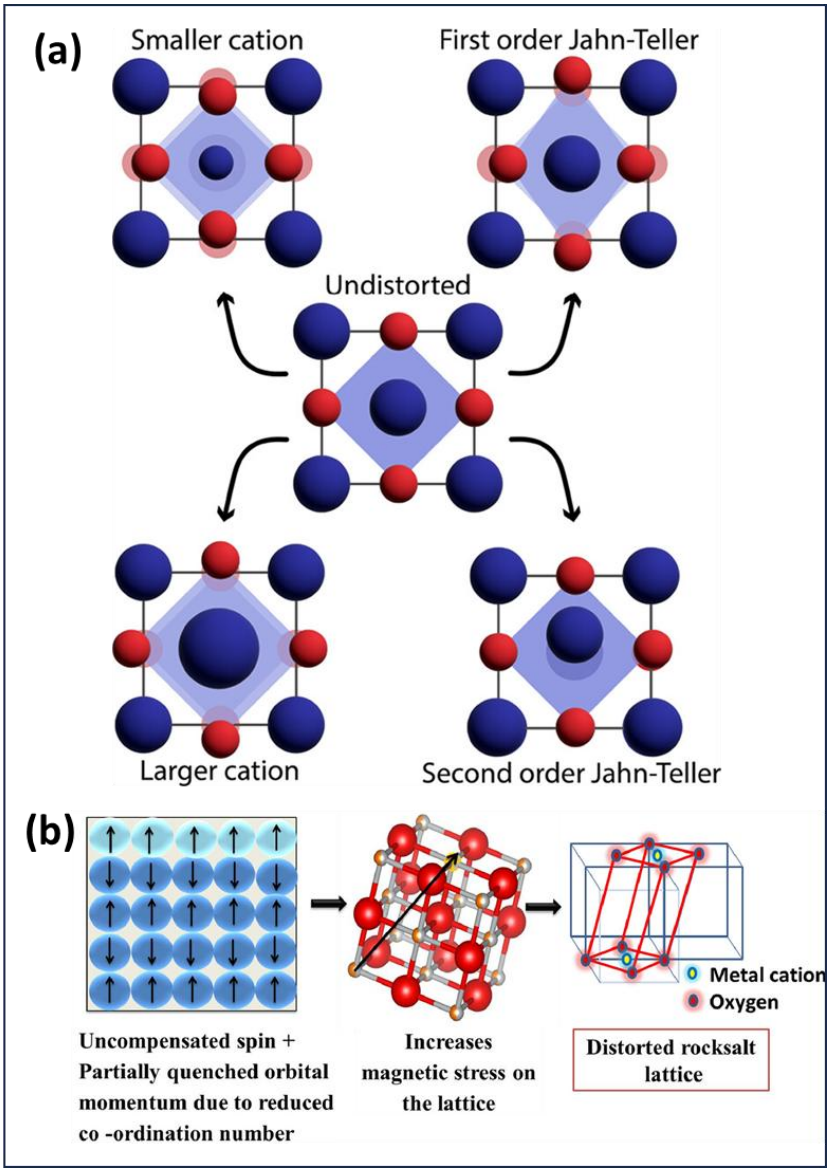


**Figure 2.6** (a) The origin of distortion in HEOs and (b) highlights distortion due to antiferromagnetism in (Mg,Co,Ni,Cu,Zn)O which causes the transformation of ideal rocksalt structure to monoclinic [115,151].

## 2.6 Functional properties

High-entropy oxides (HEOs) have emerged as the most extensively studied high-entropy ceramics in recent years. Researchers have explored their diverse properties and potential applications, including Mechanical [74,138], thermomechanical performance [66,73], catalytic activity [60,87,152–154], batteries [62,155,156], magnetic behaviour [69,92,115], electrical characteristics [25,145,157–159], and optical functionalities [160,161]. Here, we highlight the research progress in electrical and catalytic properties of HEOs.

### 2.6.1 Electrical properties

Berardan et al. [2] explored the fascinating electrical properties of (Mg,Co,Ni,Cu,Zn)O HEOs, revealing remarkable findings. When lithium was introduced into the rocksalt HEO structure, an exponential shift in electrical resistance was observed, resembling semiconductor like behaviour with a bandgap of approximately 1 eV. Interestingly, the bandgap decreased with increasing Li substitution, attributed to the creation of electroactive defects.

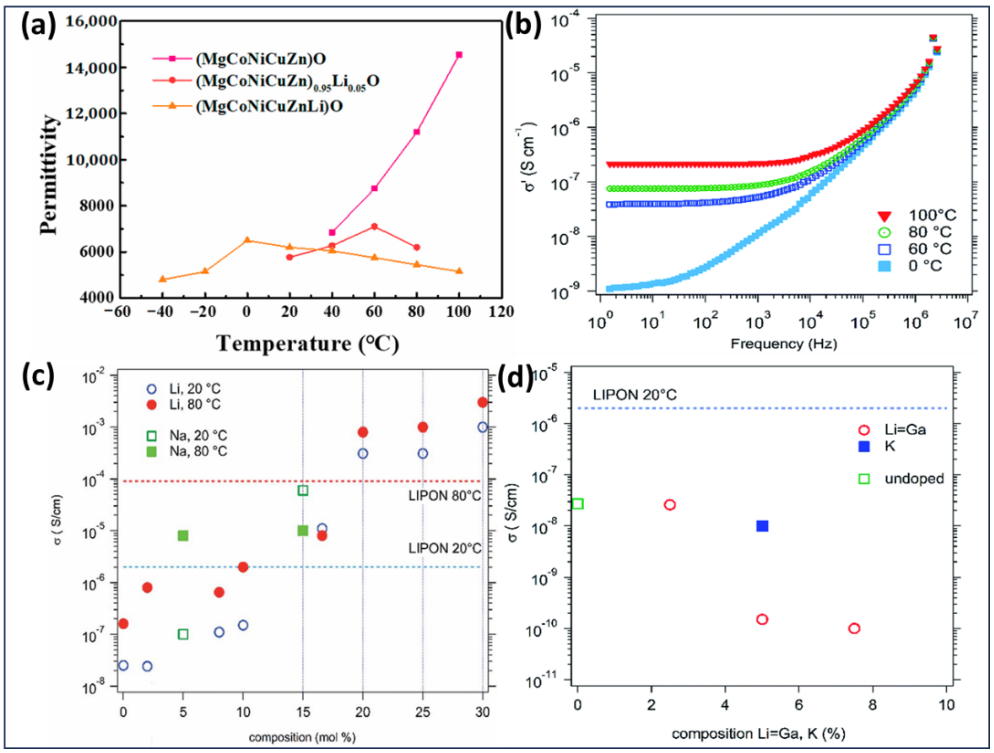


**Figure 2.7** (a) The permittivity (dielectric constant) of five components and Li added HEOs. Frequency-dependent ionic conductivity of (b) (Mg,Co,Ni,Cu,Zn)O at different temperatures (c) $(Mg,Co,Ni,Cu,Zn)_{1-x}A_x$ (A representing $Li^{1+}$, $Na^{1+}$) at 20°C and 80°C (d) $(Mg,Co,Ni,Cu,Zn)_{0.8}(Li\ Ga)_{0.2}O$ at 20°C [1,145].

These findings shed light on the complex interplay of defects and charge dynamics in HEO systems and reported CDC value of $2\times10^5$ for Li-substituted HEOs (**Figure 2.7a**). Through the experiment, they concluded that colossal dielectric constant (CDC) is the characteristics of HEO family. Berardan et al. [1,81] in another work unveiled a groundbreaking class of HEOs, conductivity of (Mg,Co,Ni,Cu,Zn)O HEO was reported $10^{-9}$ S $cm^{-1}$ (**Figure 2.7a**) using LCR meter in the frequency range of 2.3 MHz to 1.3 Hz. $(Mg,Co,Ni,Cu,Zn)_{1-x}A_x$ (A representing alkali metals like $Li^{1+}$, $Na^{1+}$) for exceptional superionic Li conductivity and rapid Na-ion

transport. These materials showed impressive $Li^+$ conductivity exceeding $10^{-3}$ S $cm^{-1}$ at ambient temperature outperforming conventional lithium phosphorus oxynitride as shown in **Figure 2.6c**. The remarkable ionic conductivity was attributed to oxygen vacancies induced by lattice distortion and charge compensation. Oxygen vacancies provide additional pathways for charge carrier hopping, inducing localized electronic states and thus increasing charge carrier concentration. However, $(Mg,Co,Ni,Cu,Zn)_{0.8}Li_{0.1}Ga_{0.1}O$ shows conductivity $10^{-8}$ S $cm^{-1}$ (**Figure 2.7d**). Gild et al.[33] reported comprehensive study on the electrical conductivity of eight fluorite-structured HEOs, revealing lower conductivities compared to $Y_2O_3$ stabilized $ZrO_2$. Notably, the inclusion of CaO further reduced conductivity at low temperatures they attributed this behavior to the influence of grain size and grain-boundary resistance, proposing that the small grain size in fluorites arising from sluggish grain growth kinetic played a key role in limiting the conductivity. These insights highlight the intricate relationship between microstructure and electrical performance in fluorite HEOs. Balcerzak et al. [126] studied the conductivity of (Mg,Co,Ni,Cu,Zn)O rocksalt HEO and achieved the highest conductivity of $8.03\times10^{-2}$ S/cm at 1148 K, as activation energy decreased from 1.01 eV (at 478 - 641K) to 0.62 eV (990-1148 K) on heating.

Several research articles reporting the dielectric properties of several different HEOs crystal structures have been published. Zhang et al. [162] analyzed that Pr substitution in (Zr,Hf,Pr,Y,La)O high entropy fluorite oxides result in cation $V_o$ complex which led to the enhanced electrical conductivity. For $(Zr_{0.1429}Hf_{0.1429}Pr_{0.1429}Y_{0.2857}La_{0.2857})O$ reported electrical conductivity at 750°C is

$1.68\times10^{-3}$ S/cm. Zhou et al. [42] synthesized $Ba(Zr_{0.2}Ti_{0.2}Sn_{0.2}Hf_{0.2}X_{0.2})O_3$, (X=Ta,Nb) perovskite HEOs via solid-state sintering method and reported dielectric constant in the range of 40-75 below 1 MHz, dielectric loss 0.15 and revealed dielectric relaxation behaviour in these HEOs. Du et al. [163] studied the dielectric constant and loss tangent of the high-entropy perovskite oxide $Ba(TiSnZrHfNbGa)_{1/6}O_3$ exhibiting frequency dispersion, indicating dielectric constant was maximum ($\varepsilon_r = 40$) at 20Hz with very low dielectric loss (0.03). Xie et al. [164] explored the high entropy effect on the dielectric properties of defective fluorite structure $(La_{0.2}Pr_{0.2}Nd_{0.2}Sm_{0.2}Eu_{0.2})Ce_2O_7$ (general formula $A_2B_2O_7$) and reported low frequency (100Hz) dielectric constant in the range of $10^5$-$10^6$ at 642°C.

### 2.6.2 Catalytic properties

(a) Photocatalytic wastewater treatment

Noble metals like platinum and rhodium are widely used in catalysis due to their unfilled d orbitals, which facilitate coordination bonds and maintain active sites[165]. Additionally, their oxidation and corrosion resistance make them ideal for catalytic applications. However, their scarcity and high cost drive the search for alternatives. Among various photocatalysts, $TiO_2$ and ZnO are the most commonly used for organic dye degradation [7,166,167]. However, their wide band gaps limit photoactivity to the UV range, which constitutes only 5% of the solar spectrum, reducing their efficiency under solar illumination. Despite efforts to enhance visible-light activity through metal or nonmetal doping, technical challenges remain [152]. Thus, the rising demand for advanced functional materials in environmental catalysis has brought entropy-stabilized oxides catalytic systems into the limelight.

By harnessing the power of entropy engineering, researchers are redefining the boundaries of functional material innovation. The remarkable potential of high entropy oxides (HEOs) in catalysis lies in their four core effects including the high entropy effect, slow diffusion effect, lattice distortion effect, and cocktail effect [168,169]. Together, these unique properties create a powerful foundation for groundbreaking advancements in catalytic performance. Dyes and heavy metals, particularly hexavalent chromium (Cr(VI)), are major pollutants that endanger aquatic ecosystems and human health. Their pervasive impact has spurred significant research in environmental protection, driving innovation in effective mitigation strategies to combat these threats. Anandkumar et al.[170] revolutionized the field of water environmental protection by pioneering the use of high-entropy oxides (HEOs) to counter water pollution. In a groundbreaking study, they introduced single-phase $Gd_{0.2}La_{0.2}Ce_{0.2}Hf_{0.2}Zr_{0.2}O_2$ (GLCHZ) and $Gd_{0.2}La_{0.2}Y_{0.2}Hf_{0.2}Zr_{0.2}O_2$ (GLYHZ) engineered with distinct bandgap values of 2.52 eV and 3.09 eV, respectively. These photocatalysts demonstrated exceptional efficiency by simultaneously reducing toxic Cr(VI) to the less harmful Cr(III) as shown in **Figure 2.8a**. They could degraded methylene blue (MB) dye within 100 minutes, marking a significant advancement in pollution mitigation strategies. Nundy et al. [32] successfully synthesized five distinct rare earth-based nanocrystalline $Ce_{0.2}Zr_{0.2}La_{0.2}Pr_{0.2}Y_{0.2}O_2$ (CZLPY) HEOs characterized by a fluorite structure achieving a 98.9% degradation of MB within 20 minute **Figure 2.8b** demonstrates mechanism of photodegradation of methylene blue using CZLPY HEO catalyst under visible light irradiation. Jia et al. [171] investigated photocatalytic degradation of tetracycline hydrochloride (TCH) using

$(La_{0.2}Ce_{0.2}Gd_{0.2}Zr_{0.2}Fe_{0.2})O_2$ as catalysts. They reported 95.4 % conversion under the visible light in 3h and attributed these findings to the defects and band structure which enables excellent charge carrier generation and migration. Usharani et al.[114] investigated the photodegradation of MB dye using (Mg,Co,Ni,Zn)O rocksalt HEOs and obtained only 18% degradation in 180 min under the illumination of Xenon lamp.

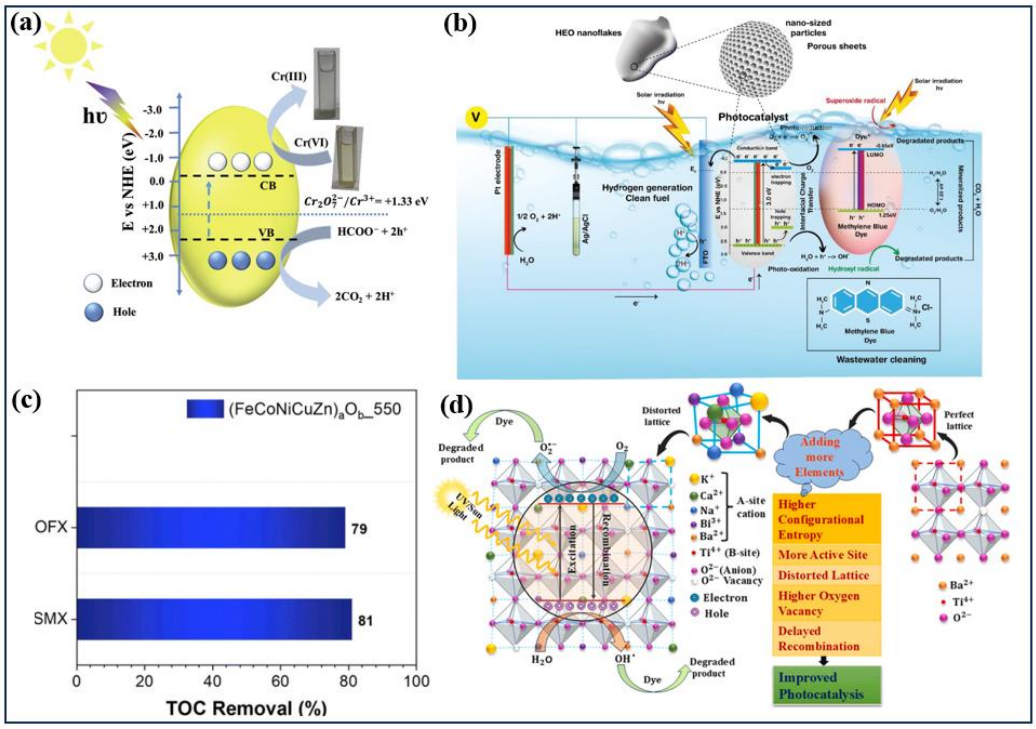


**Figure 2.8** (a) Demonstrate the mechanism of degradation of Cr (VI) to less harmful Cr (III) by GLCHZ and GLYHZ HEO catalyst (b) schematic representation of mechanism of photodegradation of Methylene blue using CZLPY HEO catalyst (c) photodegradation of Sulfamethoxazole (SMX), Oflaxocin (OFX) using (Fe,Co,Ni,Cu,Zn)O spinel NPs HEOs as catalysts (d) schematic illustrate the mechanism of photodegradation of methylene blue dye using BKCNBT high entropy perovskite as catalysts [44,166,170,172].

Das et al. [172] studied the photodegradation of Commonly used antibiotic pollutants such as sulfamethoxazole (SMX) and oflaxocin (OFX) using (Fe,Co,Ni,Cu,Zn)O spinel NPs HEOs as catalysts and reported 81% and 79% degradation (shown in **Figure 2.8c**), respectively, in 90 minutes under visible light spectrum. They attributed enhanced photocatalytic properties of (Fe,Co,Ni,Cu,Zn)O to the enhanced electronic conductivity, which facilitates efficient electron transfer. Additionally, the uniform distribution of metal cations with varying oxidation states within the HEO crystal structure activates lattice oxygen and generates reactive species for oxidation reactions, thereby supporting photocatalysis. Sharma et al. [173] investigate the structure, composition and photocatalytic characteristics of high entropy perovskite oxide (HEPO) $(Bi_{0.2}K_{0.2}Na_{0.2}Ca_{0.2}Ba_{0.2})TiO_3$ (BKNCBT). Degradation of methylene blue (MB) with rates 4.7 $\times 10^{-3}$ $min^{-1}$, $9.8 \times 10^{-3}$ $min^{-1}$ under UV light and visible light illumination, respectively was achieved. **Figure 2.8d** illustrates the mechanism of photodegradation MB dye using BKNCBT high entropy oxides catalysts.

(b) Electrocatalytic water splitting

Electrical current-driven water-splitting reactions, including the hydrogen evolution reaction (HER) and oxygen evolution reaction (OER), along with rechargeable metal-air batteries [174], represent critical advancements in energy generation and storage technologies [175]. However, the slow kinetics of the OER remains a significant challenge, even with the use of high-activity catalysts like noble metals, underscoring the need for more efficient catalytic materials. **Table 2.3** compiles previously reported work that demonstrates HEO as electrocatalyst

for water splitting. Wang et al. [181] synthesized a novel $(CoCuFeMnNi)_3O_4$ HEO with a spinel structure via solvothermal pyrolysis at 400°C. This composition marked the first application of HEOs as electrocatalysts for the oxygen evolution reaction (OER), representing a significant leap forward in catalysis.

**Table 2.3** Summary of the recently reported HEOs as OER electrocatalysts and their comparison with other electrocatalysts.

| Catalysts | Electrolyte | Overpotential (mV) at specific current density | stability | Ref |
|---|---|---|---|---|
| Pt nanowires | 1 M KOH | 520 @10 mA $cm^{-2}$ | 520 @10 $mAcm^{-2}$ | [176] |
| $CoCr_2O_4$ | 1 M KOH | 422@10mA $cm^{-2}$ | - | [177] |
| $(Co_{0.2}Ni_{0.2}Cu_{0.2}Mg_{0.2}Zn_{0.2})$ | 1M KOH | 360 @10 mA $cm^{-2}$ | 25 h | [178] |
| $NiCo\text{-}(FeCrCoNiAl_{0.1})O_x$ | 1M KOH | 391 @10 mA $cm^{-2}$ | 120 h | [179] |
| $(FeCrCoNiAl_{0.1})O_x$ | 1M KOH | 381 @10 mA $cm^{-2}$ | 120 h | [180] |
| [NO_PRINTED_FORM] | 1M KOH | 220 @10 mA $cm^{-2}$ | 9 h | [181] |

To further enhance its functionality, $(CoCuFeMnNi)_3O_4$ nanoparticles incorporated with hydrophilic multi-walled carbon nanotubes (MWCNTs), creating a hybrid material with superior conductivity and optimized mass transfer between the electrolyte and electrode. This delivered exceptional electrocatalytic performance, achieving a current density of ~10 mA $cm^{-2}$ at 1.58 V in a 1 M KOH electrolyte, showing its potential for advanced energy storage applications as shown in **Figure 2.9 (a,b)**. Talluri et al. [183] were inspired by this work and adopted a reverse co-precipitation approach to create $(CoCrFeMnNi)_3O_4$ electrocatalyst for methanol

oxidation and OER. The results show that $(CoCrFeMnNi)_3O_4$ has a specific current density of roughly 335 mA $cm^{-2}$ and a mass-activity of 110 mA $mg^{-1}$ with an observed onset potential of 0.45 V for methanol oxidation.

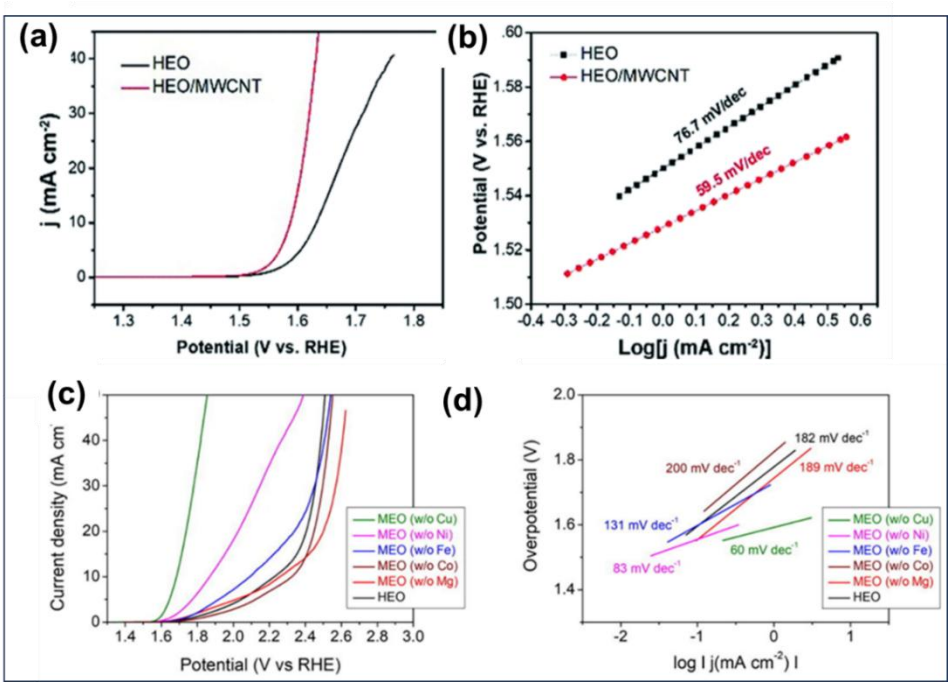


**Figure 2.9** (a) LSV polarization curve for $(CoCuFeMnNi)_3O_4$ HEO and HEO/MWCNT in 1M KOH at a scan rate of 5mV$s^{-1}$ and (b) corresponding Tafel slope from LSV curves. (c) LSV polarization curves and (d) Tafel plot for $(Mg_{0.2}Fe_{0.2}Co_{0.2}Ni_{0.2}Cu_{0.2})O$ HEO which illustrate the effect of constituent cations on the OER activity [181,182].

For the OER, the onset potential of 1.45 V versus RHE is obtained with a low overpotential of 220 mV at 10 mA $cm^{-2}$, showing highly effective electrocatalytic activity of the $(CoCuFeMnNi)_3O_4$. Kim et al. [182] investigated the OER activity of rocksalt $(Mg_{0.2}Fe_{0.2}Co_{0.2}Ni_{0.2}Cu_{0.2})O$ HEOs and unveiled the effect of constituents on OER their findings reveal that higher concentration of $Co^{3+}$ leads to

the best OER activity. **Figure 2.9(c,d)** shows the LSV polarization curve and Tafel slope for various compositions.

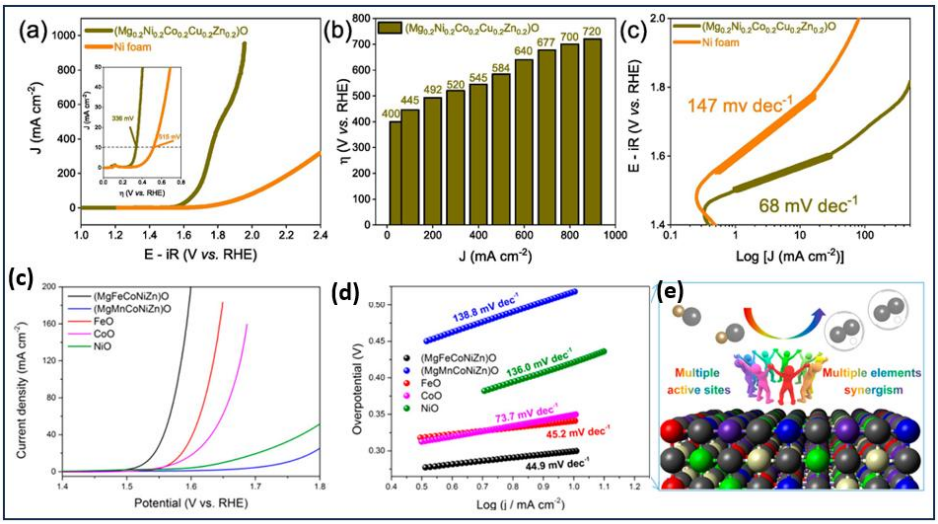


**Figure 2.10** (a) LSV curves (b) overpotential at different current density and (c) Tafel slope for (Mg,Co,Ni,Cu,Zn)O (c,d) LSV polarization curves and Tafel plot for (Mg,Fe,Co,Ni,Zn)O and (Mg,Mn,Co,Ni,Zn)O (e) schematic diagram demonstrate multiple active sites and synergistic catalysis in HEO [178,184].

Quaternary medium entropy oxides (MEOs) without Cu showed lowest overpotential of 454 mV among all the compositions as $Cu^{2+}$ prevents oxidation of $Co^{2+}/Fe^{2+}$ to $Co^{3+}/Fe^{3+}$. Santos et al. [178] evaluated the OER response of (Mg,Co,Ni,Cu,Zn)O rocksalt HEOs in OER in alkaline environment with overpotential and Tafel slope 336 mV and 68 mV/dec, respectively as shown in **Figure 2.10** (a-c). Wu et al. [184] synthesized (Mg,Fe,Co,Ni,Zn)O, (Mg,Mn,Fe.Co,Ni)O rocksalt HEO using joule heating approach which showed lower overpotential close to 300mV/dec and Tafel slope 44.9 mV/dec indicating the positive synergetic effect of elements combination for OER as shown in **Figure**

**2.10 (c,d)**. They ascribed the role of Fe and Co in improving the OER activity. **Figure 2.10(e**) shows the schematic of multiple element synergy in HEOs which enhanced the electrocatalytic activity. Hong et al. [16] explored the electrocatalytic OER activity (in 1M KOH) of (Mg,Fe,Co,Cu,Zn)O rocksalt HEO at different calcination temperature. They concluded that at calcination temperature up to 1200°C overpotential (430) mV and Tafel slope (77 mV/dec) decreased while (electrochemical surface area) ECSA increased. However minimum overpotential (430 mV) and Tafel slope (70 mV/dec) were achieved for HEO catalysts calcined at 1300°C owing to enhanced crystallinity. Zhang et al. [185] synthesized $(Co,Ni,Mn,Zn,Fe)_3O_{3.2}$ using electrospinning technique which exhibit overpotential of 336 mV at 10 $mAcm^{-2}$ and Tafel slope of 47.5 mV $dec^{-1}$ in OER process. Chronoamperometry test showed that high entropy oxides keep its electrocatalytic stability up to 25 hours. Zhang et al. [186] investigated electrocatalytic OER response of $(Co_{0.25},Ni_{0.25},Mn_{0.25},Zn_{0.25})Fe_2O_4$ spinel type HEO which showed an overpotential of 276 mV at a current density 10 $mAcm^{-2}$.

Various research papers have significantly contributed to the fundamental understanding of high-entropy oxides (HEOs), shedding light on their unique structural, electronic, and thermodynamic properties. These studies have provided valuable insights into the entropy stabilization mechanism, defect chemistry, phase stability, and the influence of diverse cation combinations on functional properties. Additionally, extensive research has explored the synthesis methods, from conventional solid-state reactions to advanced techniques like sol-gel, co-

precipitation, and pulsed laser deposition, enabling better control over composition and microstructure.

Beyond fundamental studies, numerous investigations have highlighted the vast potential of HEOs in a wide range of applications, including catalysis, energy storage, and electronic devices. Research in electrocatalysis has demonstrated how HEOs can serve as highly efficient catalysts for photodegradation and oxygen evolution reactions (OER), offering a viable alternative to costly noble metal catalysts.

As the field continues to evolve, each new study enriches the ever-expanding knowledge base on high-entropy oxides, bridging the gap between theory and application. These collective efforts are not only deepening our fundamental understanding of HEOs but also paving the way for their integration into real-world technologies, further strengthen their role in the future of materials science and sustainable innovation.

## 2.7 Conclusions

The aforementioned study on high entropy oxides highlights the enthalpy-driven stabilization as entropy can be manipulated in terms of both compositional complexity and structural disorder thus widening the range of various functional properties and applications. High $\Delta S_{mix}$ associated with mixing five or more near-equimolar metal elements or ions thermodynamically favors the synthesis of a single-phase solid solution. Subsequent research has revealed that various thermodynamic, structural parameters, and kinetic factors play a key role in

designing single-phase crystalline solid solutions. When considering the charge compensation mechanism to accommodate large size cation or aliovalent cation substitution any composition should contain multivalent cations because the presence of multivalent cation in any composition decides the level of charge natality compensation mechanism. Various studies revealed that to accommodate large-size cation oxygen stoichiometry is an essential factor. In some studies, it has been observed that Hume Rothery and Paulling's rule regarding size limitation and the same oxidation states of cation are not essential criteria for the formation of phase pure crystal structure. Overall, from a fundamental standpoint, these various phase stability mechanisms make HEOs special which encourages more investigation to better understand the causes of phase stability in HEOs. Compensating mechanisms greatly influence compositional stability, desired qualities, rational design, and composition optimization to achieve targeted properties.